Supplementary information for: Satellites detect methane outburst driven by magma-sediment interactions

Dualeh, EW[1]*, Biggs, J[1], Sharma, S[2], Stix, J[3], Hutchison, W[4], Etiope, G[5,6], Jervis, D[7],Way, L[1], Dogniaux, M[2], Maasakkers, J.D[2], Aveni, S[8,9], Cusworth, D[10], Ireland, B[1], Grandin, R[11], Girard, M[7], Ramier, A[7], Zheng, W[1], Davis, T[1], Howell K[10,12], Coppola, D[8], Hauck, A[11], Pancost, RD[1], Nettles, M[13], Lewi, E[14].

[1*]COMET, School of Earth Sciences, University of Bristol, Bristol, UK; [2]SRON Space Research Organisation Netherlands, Leiden, Netherlands; [3]Department of Earth & Planetary Sciences, McGill University, Canada; [4]School of Earth and Environmental Sciences, University of St Andrews, St Andrews, UK; [5]Istituto Nazionale di Geofisica e Vulcanologia (INGV), Rome, Italy; [6]Faculty of Environmental Science and Engineering, Babes-Bolyai University, Cluj-Napoca, Romania; [7]GHGSat Inc., Montreal, Quebec, Canada; [8]Department of Earth Sciences, University of Turin, Turin, Italy; [9]Department of Civil, Constructional and Environmental Engineering (DICEA), Sapienza University of Rome, Rome, Italy; [10]Carbon Mapper, Pasadena, United States; [11]Institut de physique du globe de Paris (IPGP), Université Paris Cité, CNRS, Paris, France; [12]College of Engineering, University of Michigan, Michigan, ISA; [13]Lamont-Doherty Earth Observatory (LDEO), Columbia University, Palisades, USA; [14]Institute of Geophysics, Space Science and Astronomy, Addis Ababa University, Addis Ababa, Ethiopia

*Corresponding author(s). E-mail(s): edna.dualeh@bristol.ac.uk

Content of this file

Supplementary text S1 to S5

Table S1 to S9

Figures S1 to S20

Introduction

This supporting information includes the following:

1. Detailed results of methane and carbon emissions from satellite instruments (Text S1, Figure S1-S5 and Table S1-S5)
2. Detailed results of deformation analysis and modelling (Text S2, Figure S6-S10 and Table S6-S8)
3. Detailed timeline of thermal anomaly evolution (Text S3 and Figure S11-S13)
4. Detailed description of changes in optical imagery (Text S4 and Figure S14-S15)
5. Detailed comparison of methane and carbon dioxide in the East African Rift (Text S5, Figure S16-20 and Table S9)

Supplementary Text S1 Satellite-based gas measurements

We analyze a total of 27 methane emission rate estimates quantified using satellite observations from TROPOMI (Fig. S1), GHGSat (Fig. S3), and Carbon Mapper's Tanager (Fig. S4) instrument to construct a comprehensive timeline of emissions from Fentale Volcano (Fig. S5). The first methane plume was detected by TROPOMI on 19 January 2025, while the final observation comes from GHGSat on 9 April 2025. As summarized in Table S4, we have 7 methane plume observations from TROPOMI, 17 from GHGSat, and 3 from Tanager.

To estimate the total methane mass released over the course of the event, we use a smoothing spline approach employing the Generalized Cross Validation (GCV) criterion to fit a smoothing basis spline to the emission rate timeseries. The total emission estimate is then calculated as the area under the resulting curve, providing an integrated estimate of the methane released over time.

Given the associated uncertainty in the emission estimates, we propagate this uncertainty through a Monte Carlo simulation with 10000 iterations. In each iteration, the emission estimates are randomly perturbed following normal distributions using the reported uncertainties as standard deviation, and a new smoothing spline is fitted to the perturbed data. This process generates an ensemble of area under the curve (AUC) (total emission) estimates. Additionally, we fit two alternative models, an exponential function and a 6th-order polynomial, using the same perturbed data, and compute the corresponding AUCs for each model. These alternative models provide complementary uncertainty estimates and are incorporated into the uncertainty ensemble. The final uncertainty in the total emission estimate is quantified by calculating the standard deviation of the AUC estimates obtained from the Monte Carlo simulations. This robust uncertainty estimate accounts for both the variability in the individual emission observations and the different model assumptions used in the fitting process.

Integrating the fitted emission curve yields a total release of 37.7 ± 3.9 kt of methane over the observed period, spanning from the first TROPOMI detection on 19 January 2025, to the final GHGSat overpass on 9 April 2025 (Fig. S4). No methane plumes were detected at Fentale Volcano in TROPOMI data prior to 19 January (Fig. S2). To better constrain the onset of the release, we performed a back-trajectory analysis using planetary boundary layer averaged ERA5[1], NCEP[2] and GEOS-FP[3] wind fields. By tracking the most downwind TROPOMI plume pixel of the 19 January plume back to Fentale Volcano, we estimate that emissions likely began at least 4-6 hours before the TROPOMI overpass time (10:26 UTC) on 19 January. To account for methane released between this inferred onset and the first TROPOMI observation, we conservatively add the plume mass observed on 19 January (0.5 kt) to the integrated estimate. This adjustment yields a total emission estimate of 38.2 ± 3.9 kt, representing the best-constrained estimate of methane released during the Fentale event.

Table S1. *Planetary boundary layer scheme options used for the WRF-Chem simulations.*

WRF PBL Scheme Option	Description
1	Yonsei University Scheme (YSU)[4]
2	Mellor–Yamada–Janjic Scheme (MYJ)[5]
4	Quasi–normal Scale Elimination Scheme (QNSE)[6]
5	Mellor–Yamada Nakanishi Niino Level 2.5 (MYNN2)[7]

Table S2. *Variations in key inputs and assumptions used to construct the inversion uncertainty ensemble for TROPOMI-based emission quantification.*

Parameter	Base inversion	Ensemble variations considered
Aggregation resolutions	0.1°	Native TROPOMI resolution and 0.20°
CAMS boundary conditions uncertainty	10%	1%
Prior uncertainties	100%	50% and 150%.
TROPOMI data quality	qa value ≥ 0.4	qa value = 1
Albedo filtering	SWIR surface albedo > 0.05	Removing the albedo filtering criteria
Error characterization	Using the central limit theorem	Using the mean observational error
Prior scaling factor	1	0.5, 1.5
Temporal sampling	Sampling model outputs at TROPOMI overpass hour	Simulation outputs sampled one hour before and after the TROPOMI overpass hour
Plume match selection	Using best plume match based on observation cost	Using second-best plume match based on observation cost
		Plume matches selected from simulations using meteorological drivers restricted to NCEP or ERA5 only
		Using the plume match corresponding to the maximum emission rate estimated from the preliminary inversion
TROPOMI methane product	TROPOMI-GOSAT blended product	Performing the inversion using the TROPOMI operational product

Table S3. *Quantified daily emission rates for TROPOMI-observed plumes, estimated using the Integrated Mass Enhancement (IME) method and a Bayesian inversion framework. Q_{IME} and σ_{IME} represent the emission estimates and associated uncertainties from the IME method, respectively. Q_{INV} and σ_{INV} denote the posterior emission estimates and their 1-σ uncertainties derived from the Bayesian inversion.*

Observation date	TROPOMI Orbit No.	Q_{IME} (t/hr)	σ_{IME} (t/hr)	Q_{INV} (t/hr)	σ_{INV} (t/hr)
2025/01/19	37668	126	40	157	41
2025/01/22	37711	76	27	88	19
2025/01/23	37725	92	32	82	14
2025/01/28	37796	52	19	57	9
2025/02/08	37952	34	13	42	9
2025/02/19	38108	Not detected		45	16
2025/02/20	38122	26	9	21	20

Table S4. *Fentale Volcano daily methane emission rates derived for individual plumes observed by TROPOMI, GHGSat, and Carbon Mapper (Tanager), with associated uncertainties.*

Observation date & time (UTC)	Emission Rate (t/hr)	Uncertainty (t/hr)	Instrument
19/01/2025 10:26	157.4	40.8	TROPOMI
22/01/2025 11:10	88.2	18.9	TROPOMI
23/01/2025 10:51	82.2	14.3	TROPOMI
28/01/2025 10:57	56.6	9.2	TROPOMI
31/01/2025 07:59	62.8	36.0	GHGSat
01/02/2025 07:56	16.5	9.1	GHGSat
06/02/2025 06:08	2.1	1.2	GHGSat
06/02/2025 11:21	19.5	11.0	GHGSat
08/02/2025 08:17	21.0	15.6	Carbon Mapper
08/02/2025 10:51	42.1	9.5	TROPOMI
09/02/2025 08:03	32.3	19.3	GHGSat
15/02/2025 08:15	20.3	12.0	Carbon Mapper
16/02/2025 06:16	11.0	6.2	GHGSat
18/02/2025 08:00	27.4	17.2	GHGSat
19/02/2025 10:45	45.0	16.1	TROPOMI
20/02/2025 07:58	1.3	0.7	GHGSat
20/02/2025 10:26	21.5	20.5	TROPOMI
22/02/2025 08:16	12.2	5.2	Carbon Mapper
23/02/2025 06:12	3.9	2.3	GHGSat
26/02/2025 08:02	1.8	1.8	GHGSat
27/02/2025 08:00	7.1	4.1	GHGSat
04/03/2025 08:01	0.5	0.3	GHGSat
12/03/2025 11:27	3.1	1.9	GHGSat
15/03/2025 11:22	1.9	1.1	GHGSat
16/03/2025 11:25	3.0	1.9	GHGSat
01/04/2025 06:10	0.4	0.2	GHGSat
09/04/2025 07:57	2.7	1.6	GHGSat

Table S5. *Fentale Volcano carbon dioxide emission rates derived for individual plumes observed by Carbon Mapper (Tanager), with associated uncertainties. *Addition of potentially two distinct sources.*

Observation date & time (UTC)	Emission Rate (t/hr)	Uncertainty (t/hr)	Instrument
08/02/2025 08:17	15,100	11,000	Carbon Mapper
15/02/2025 08:15	5,730	3210	Carbon Mapper
22/02/2025 08:16	7,900*	3900	Carbon Mapper

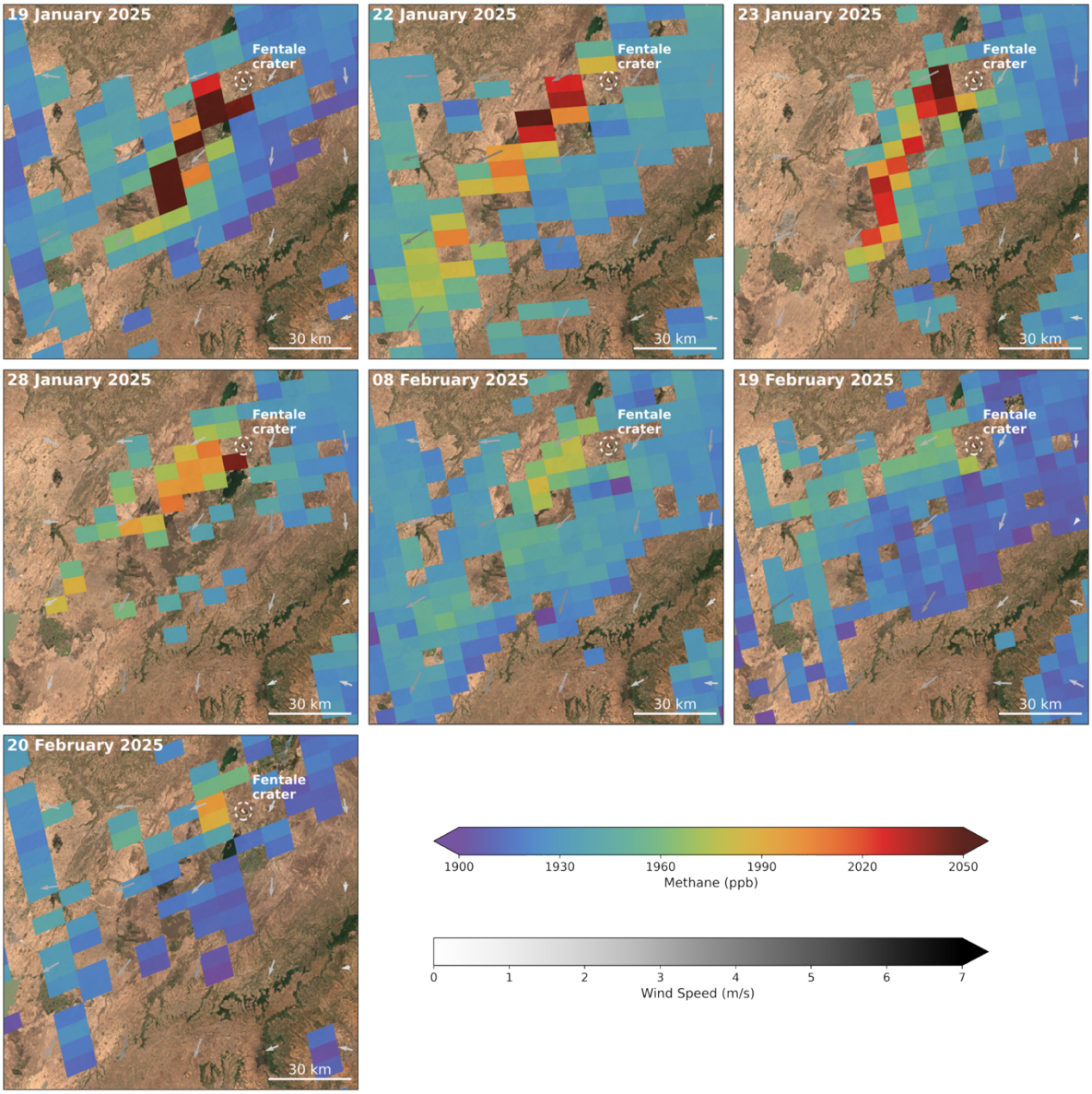

Figure S1. *TROPOMI methane column concentration maps showing plume observations over Fentale Volcano. Data are based on the operational TROPOMI-CH_4 product (version 02.05.00). The color scale represents the total methane column concentration, while arrows indicate 10-m wind direction and intensity based on ERA5[1]. Sentinel-2 RGB imagery from 22 January 2025 is shown as the background.*

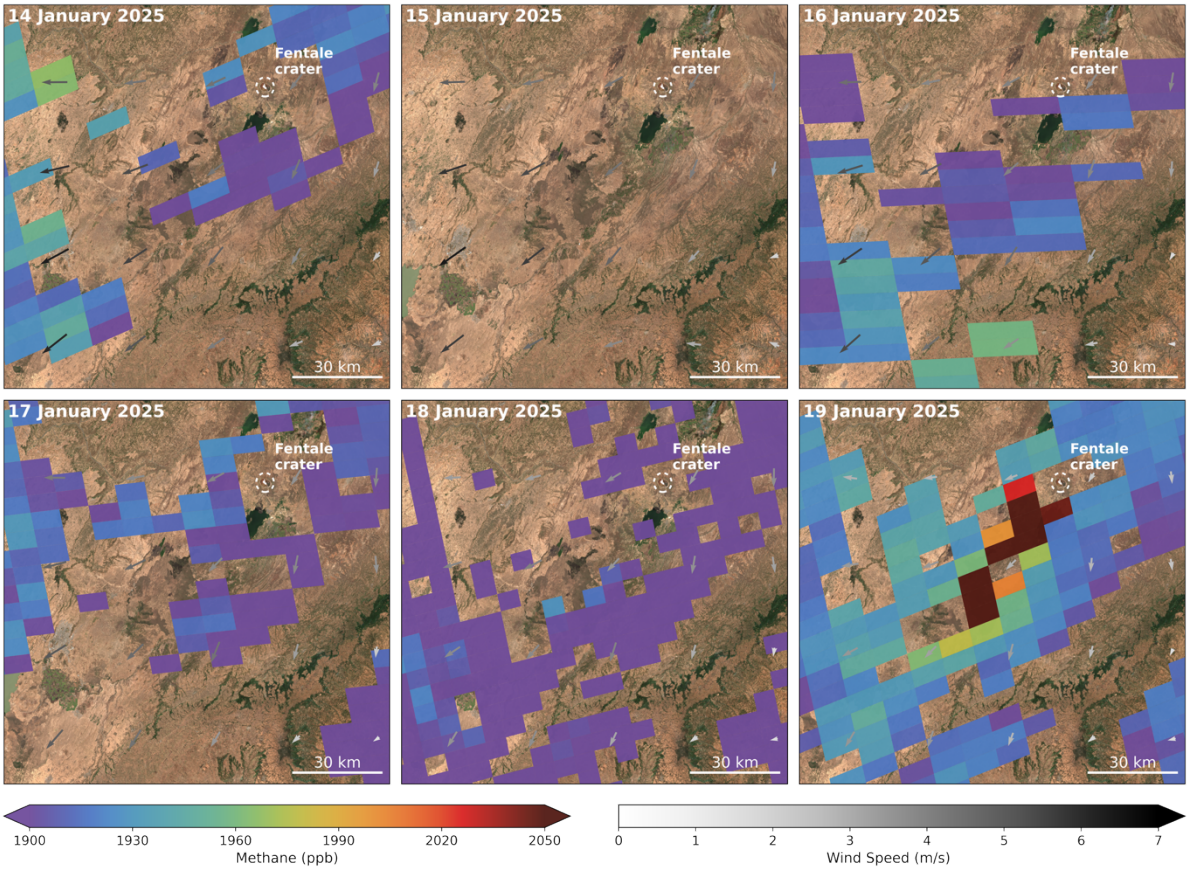

Figure S2. *TROPOMI methane column concentration maps showing observations prior to methane detection at Fentale Volcano. Data are based on the operational TROPOMI-CH_4 product (version 02.05.00). The color scale represents the total methane column concentration, while arrows indicate 10-m wind direction and intensity based on ERA5[1]. Sentinel-2 RGB imagery from 22 January 2025 is shown as the background.*

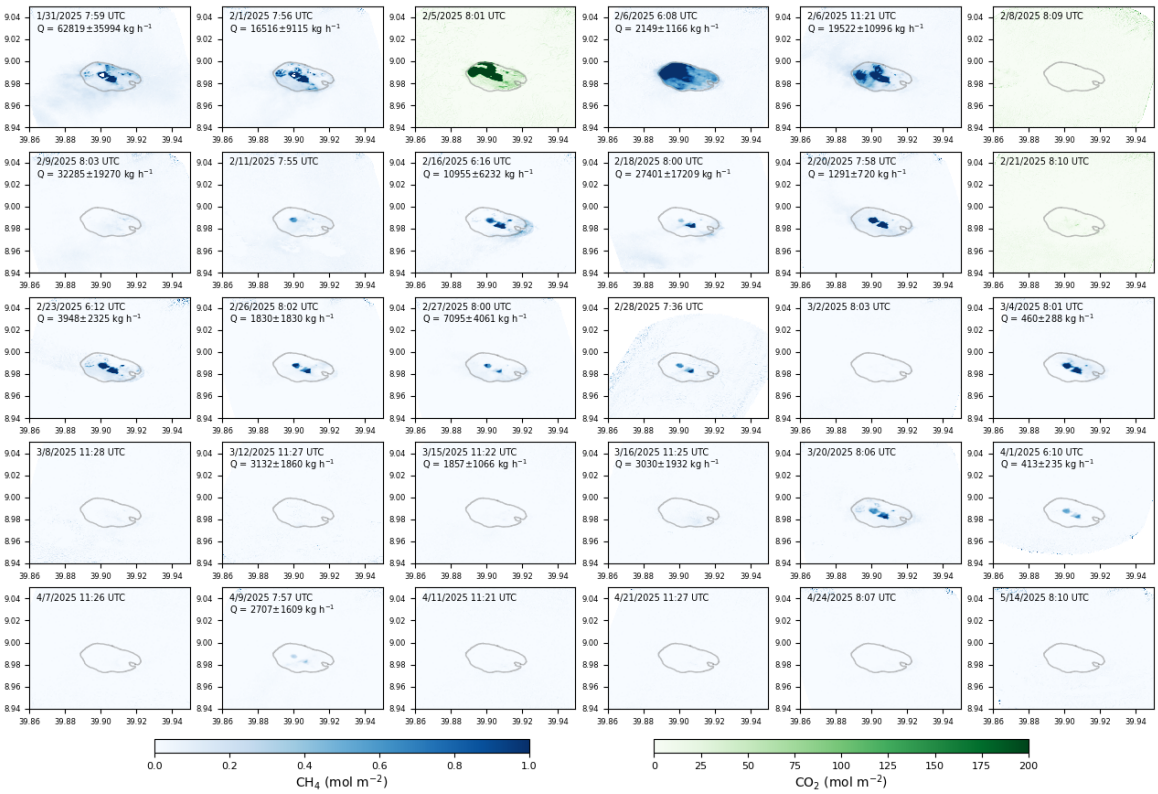

Figure S3. *GHGSat column density enhancement measurements between 31 January 2025 and 14 May 2025. Methane enhancement measurements are shown in blue, CO_2 measurements are shown in green. For measurements where an emission enhancement was detectable outside of the crater (grey line), an emission rate was estimated (and annotated in the plot).*

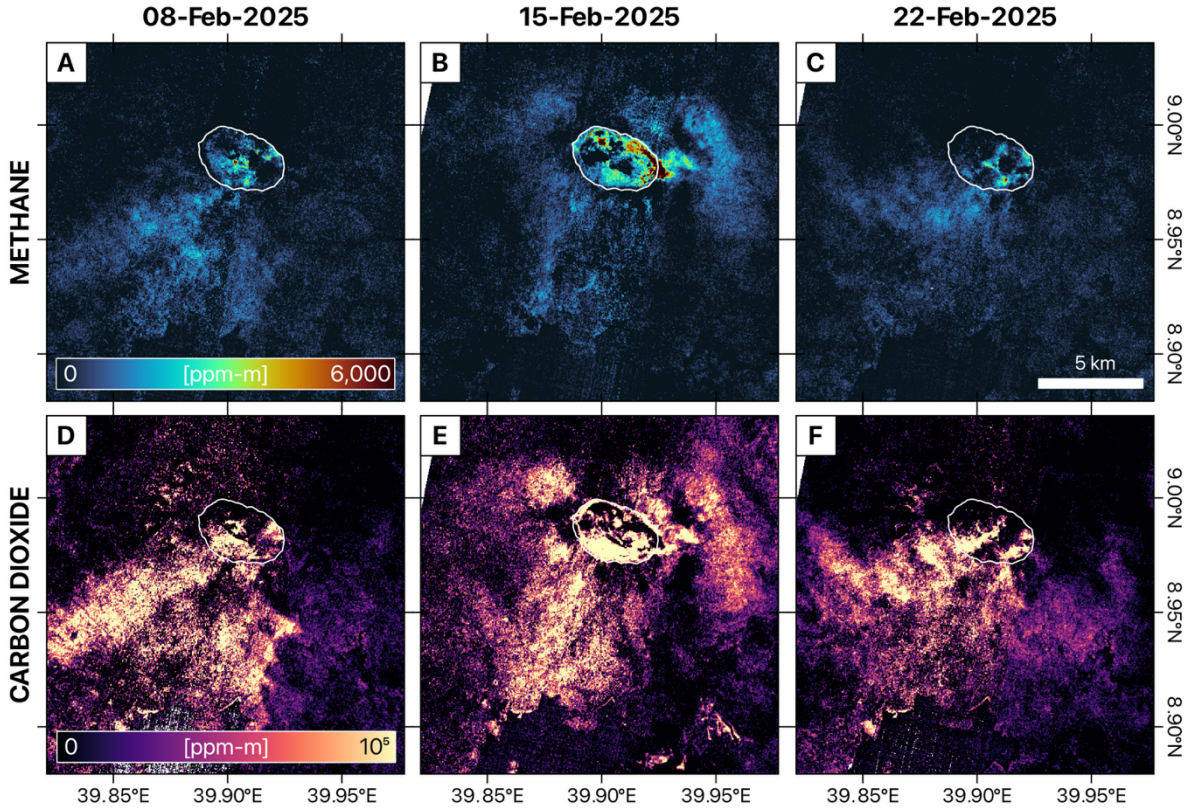

Figure S4. *Carbon Mapper Tanager-1 column concentration maps of methane (top row) and carbon dioxide (bottom row) showing plume observations over Fentale Volcano in February 2025.*

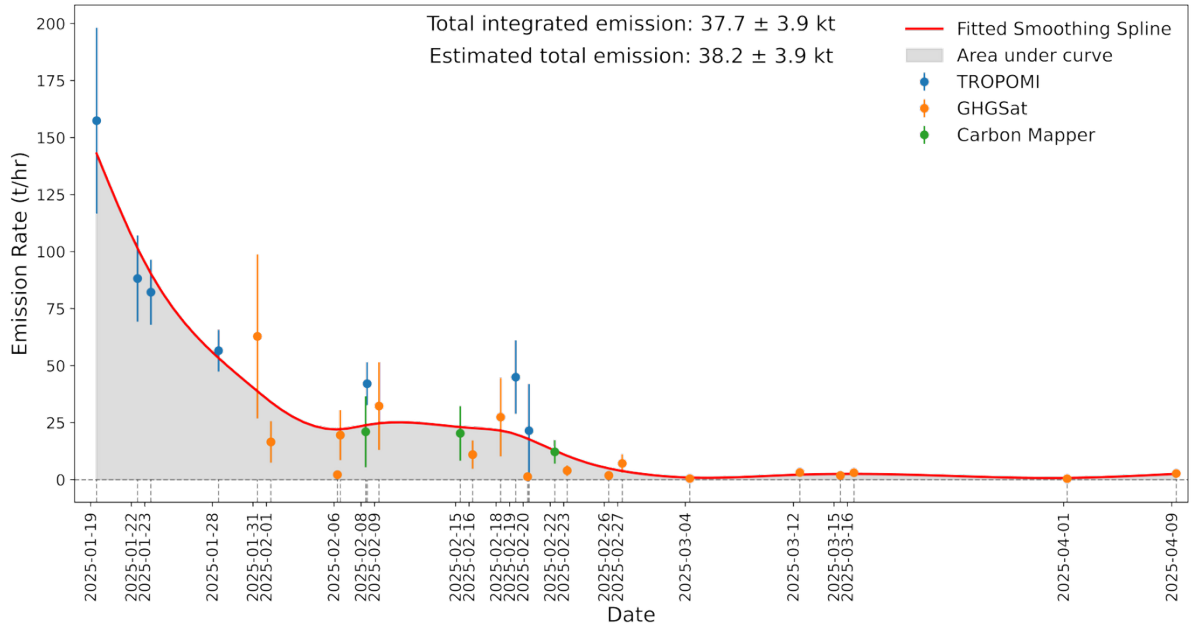

Figure S5 *Timeline of methane emission rates from Fentale, based on 27 satellite plume observations from TROPOMI (7), GHGSat (17), and Tanager (3). A smoothing spline fit to the data gives a total integrated emission estimate of 37.7 ± 3.9 kt between 19 January and 9 April 2025. To account for the inferred start of emission occurring 4-6 hours before the TROPOMI overpass at 10:26 UTC on January 19, the total emission estimate of 38.2 ± 3.9 kt includes an additional 0.5 kt from the plume mass observed on January 19. This adjusted figure represents the best-constrained total release estimate.*

Supplementary Text 2 Synthetic Aperture Radar deformation analysis

Individual interferograms over Fentale Volcano clearly show two overlapping deformation signals (Figure S6): (1) a broad subsidence signal beneath Fentale and (2) a localised subsidence signal in the southeast portion of Fentale crater (Fig. S6). Deformation timeseries between December 2024 and 9 February 2025 (Fig. S7A, D) show a broad subsidence signal outside of Fentale (towards the southwest in ascending and northeast in descending track). This subsidence signal coincides with the onset of the dyke emplacement between the 17-30 December 2024 and has a total of ~70 cm of subsidence in the satellite's line-of-sight (LOS) by February 2025. From the individual interferograms (Fig. S6), we know there is an overlapping localised subsidence signal in the crater. Using the anomaly detection method described in Giudicepietro et al., (2024)[8], we are able to extract the smaller magnitude signal (Fig. S7C, F). The temporal trend of this localised signal differs from the broad signal, and correlates strongly with the detection of the methane emissions on the 19 January 2025 (Fig. S7). However, as the extent of the two subsidence signals overlap, there may still be a proportion of mixing occurring between the two signals. We estimate LOS subsidence of -12.5 ± 0.9 cm (ascending) and -30.8 ± 2.3 cm (descending) between the 15 and 23 January 2025.

The inversion using an Okada source model using both ascending and descending track fit the signal well (RMS 2.4 cm and BIC 272; Table S7). The source for the localised subsidence signal was modelled at a depth of 278 m (257-363 m, 95% confidence) with a volume of 1.55×10^5 m^3 (-2.01 to -1.38×10^5 m^3, 95% confidence) (Table S8). Using these model parameters, we estimate the source volume through time for both CSK tracks, this shows that the localised subsidence signal began between 16-23 January 2025 (Fig. S9). The majority of the volume change coinciding the methane emission detection.

Following the ~40 m collapse on the 14 February 2025, we continue to observe subsidence in the southeast portion of the crater. The spatial footprint and pattern are different, with a decrease in displacement rates, with some areas stabilising completely by March and the majority of observed subsidence concentrated along the edge of the collapse footprint (Fig. S10).

Table S6. *Synthetic Aperture Radar (SAR) data used for deformation analysis of Fentale Volcano Ethiopia, divided into two timeframes, (1) the period from December 2024 until the large m-scale crater collapse on the 14 February that observes the localised cm-scale crater deformation and (2) any deformation following the mid-February collapse event.*

Generation	Direction	Track ID	Heading (°)	Incidence angle (°)	Timeframe	Date Range	Images used
CSK	Descending	H4_04	192	32	Pre	05/12/2024 – 08/02/2025	10
	Ascending	H4_02	-11	27	Pre	06/12/2024 – 09/02/2025	9
					Post	17/02/2025 – 01/06/2025	12
CSG	Ascending	STR004	-12	27	Post	23/02/2025 – 23/06/2025	15
	Descending	STR006	192	32		22/02/2025 – 22/06/2025	15

Table S7. *Results of systematic examination of potential sources to model localized deformation signal at Fentale Crater. Compound Dislocation Model (CDM). Bayesian Information Criterion (BIC).*

Source type	Model Code	RMS [cm]	Delta BIC vs. Mogi [Weighted]	Delta BIC vs. Mogi [Unweighted]
CDM-based planar sill (with elongation)	CDMJ	2.35	267.39	3115.20
Okada Sill[9]	SILL	2.36	272.25	3092.85
Very shallow penny crack[10]	SUNV	2.69	116.97	2196.14
CDM-based planar sill (no elongation)	CDMI	2.76	106.32	2015.99
Oblate CDM	CDMO	3.56	75.04	188.68
Mogi[11]	MOGI	3.68	0.00	0.00
Cervelli spheroid[12]	CERV	4.00	117.25	-630.91
Prolate CDM	CDML	4.07	46.10	-757.42

Table S8. *Optimal output model parameters for top preferred sources investigated. Optimal Value, superscript 97.5 percentile, subscript 2.5 percentile. X and Y are distance from point (39.890°E, 8.972°N).*

Source type	CDMJ	SILL	SUNV	CDMI
RMS [cm]	2.4	2.4	2.7	2.8
X	2667^{2717}_{2643}	3164^{3229}_{3107}	2671^{2721}_{2621}	2662^{2721}_{2618}
Y	1050^{1080}_{1019}	852^{942}_{811}	1033^{1065}_{990}	1019^{1060}_{983}
Depth [m]	300^{350}_{256}	278^{363}_{257}	294^{462}_{258}	368^{521}_{310}
Volume [$\times 10^5$ m^3]	$-1.60^{-1.40}_{-2.02}$	$-1.55^{-1.38}_{-2.01}$	$-1.64^{-1.31}_{-2.17}$	$-1.76^{-1.36}_{-2.34}$
X Radius / Length [m]	321^{365}_{287}	641^{699}_{589}	[Radius]	[X/Y Radius]
Y Radius / Width [m]	519^{551}_{473}	1053^{1113}_{959}	534^{564}_{307}	386^{412}_{307}
Strike [°]	110^{118}_{104}	21^{27}_{12}	-	-
Opening [m]	-	$-0.23^{-0.20}_{-0.31}$	-	-

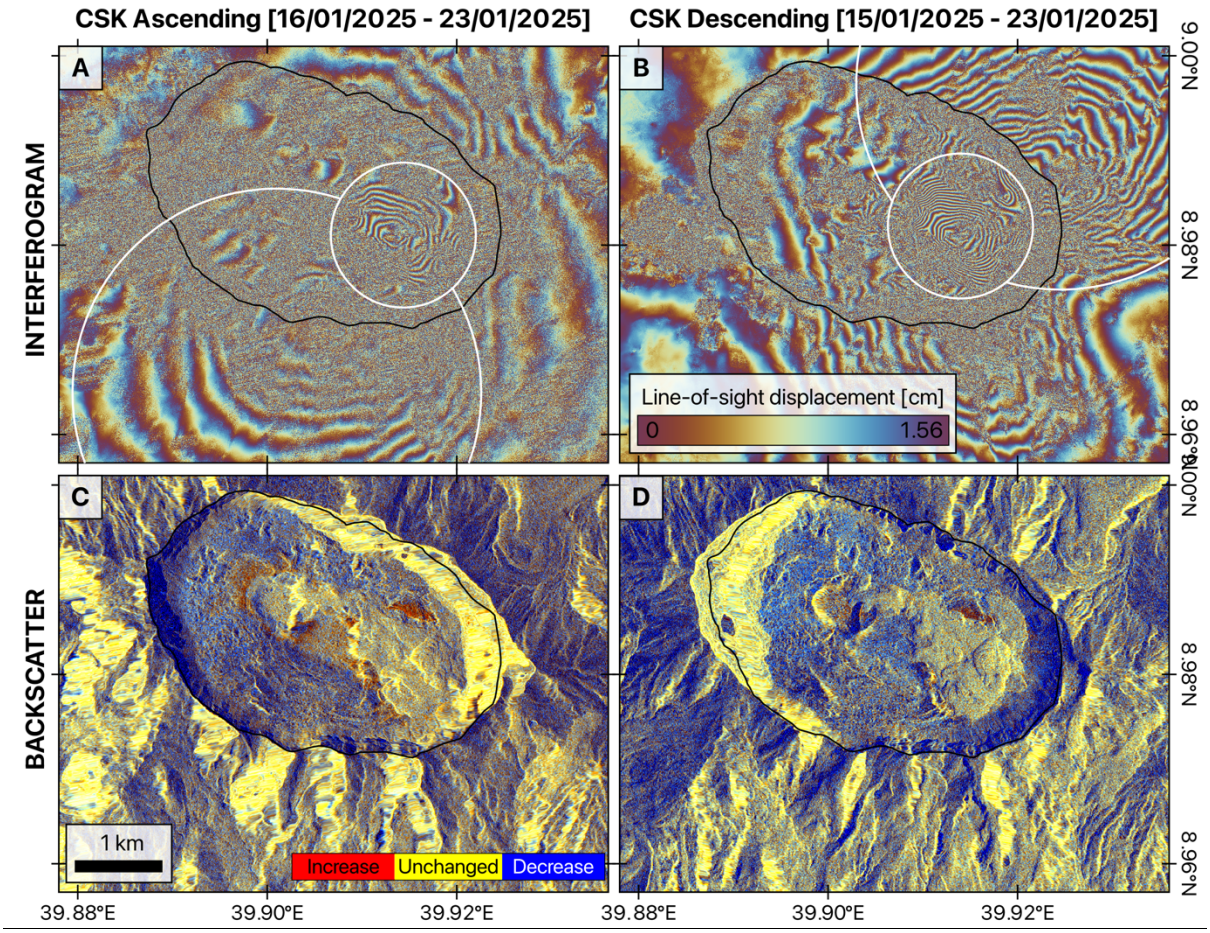

Figure S6. *COSMO-SkyMed (CSK) Synthetic Aperture Radar (SAR) images acquired over Fentale Volcano from ascending (A-C) and descending (B-D) tracks. Individual interferograms (A-B) showing broad subsidence signal beyond caldera (large white circle) and localised subsidence signal (small white circle) within caldera. Corresponding change difference backscatter images showing changes large increases in signal within Fentale Crater. The caldera is shown in black.*

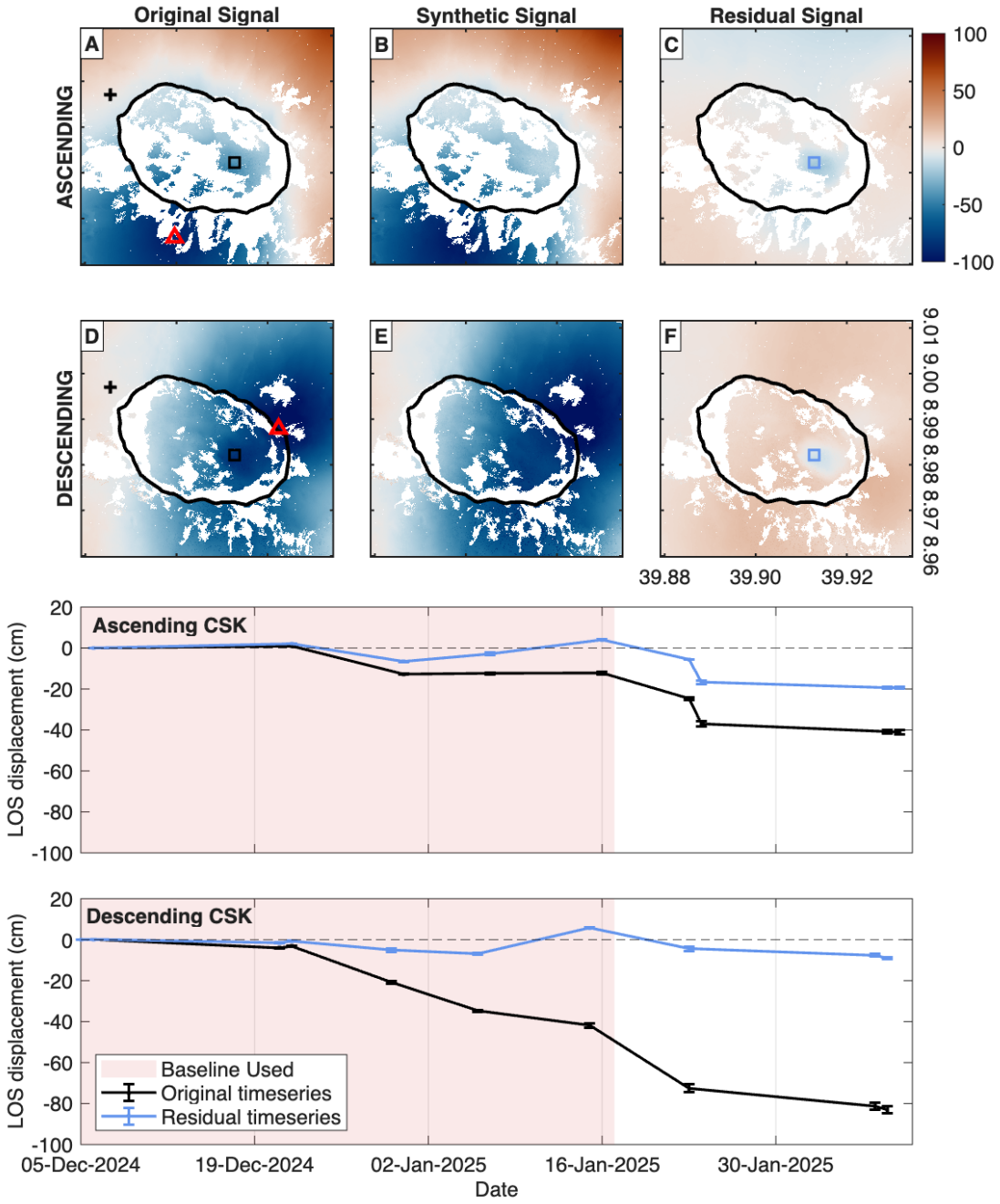

Figure S7. *Total line-of-sight (LOS) deformation timeseries for (A) ascending and (D) descending COSMO-SkyMed (CSK) interferograms over Fentale volcano, Ethiopia. Deformation observed shows the combined signal of the localised and widespread subsidence signals occurring at Fentale between 05 December 2024 and 14 February 2025. Panels (B and E) show the constructed synthetic signal using method described in Giudicepietro et al., (2024)[8] and (C and F) is the residual between the original and synthetic signal used to extract the localised subsidence signal within Fentale. The timeseries show the original total (black) and anomaly or localised (red) LOS deformation for the ascending (top timeseries panel) and descending (bottom timeseries panel) CSK data. The timeseries are mean of a 5×5 pixel window with standard deviation shown, centre pixels are shown on panel (A – black square) and (C – blue square). All shown deformation signals are in cm and difference in magnitude location of subsidence are related to being observed in the LOS of the satellite. Timeframes used as input for background deformation levels for anomaly detection method shown as pale red area on timeseries plots.*

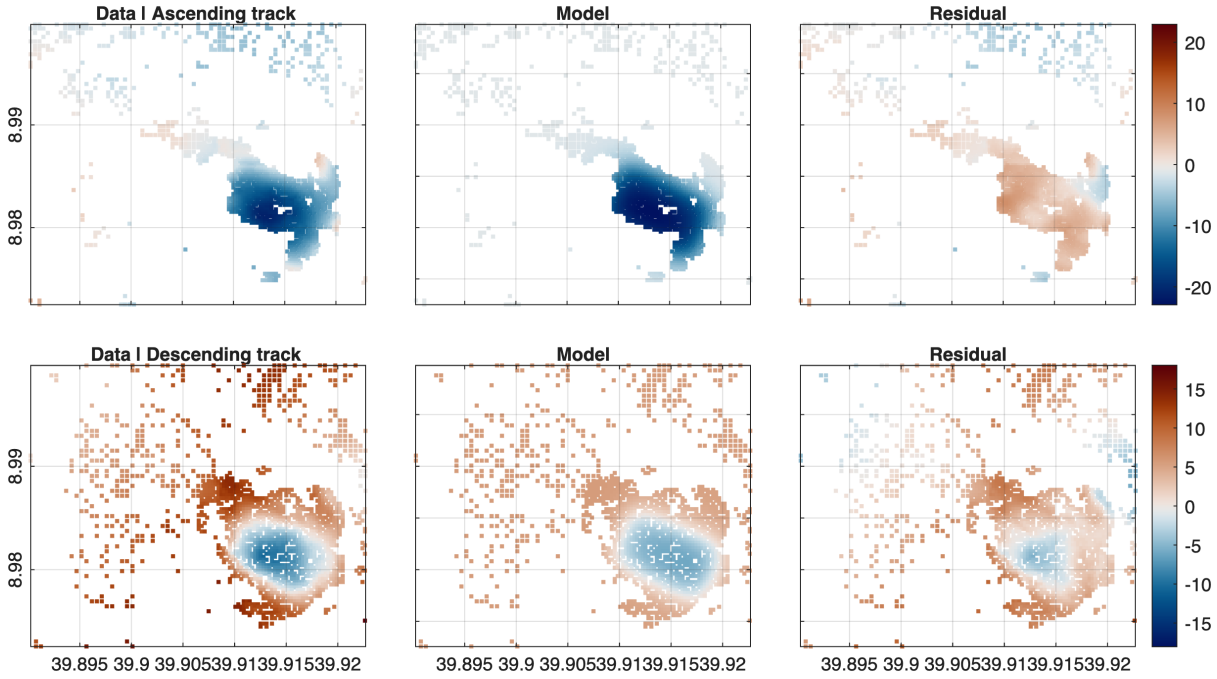

Figure S8. *Data-model-residual plot for sill source inversion at Fentale using ascending (top row) and descending (bottom row) deformation images from cumulative deformation extracted in S7 (between 05 December 2024 and 14 February 2025). Model uses the optimal output model parameters for a sill shown in Table S8. Displacement is shown as line-of-sight displacement in cm-scale.*

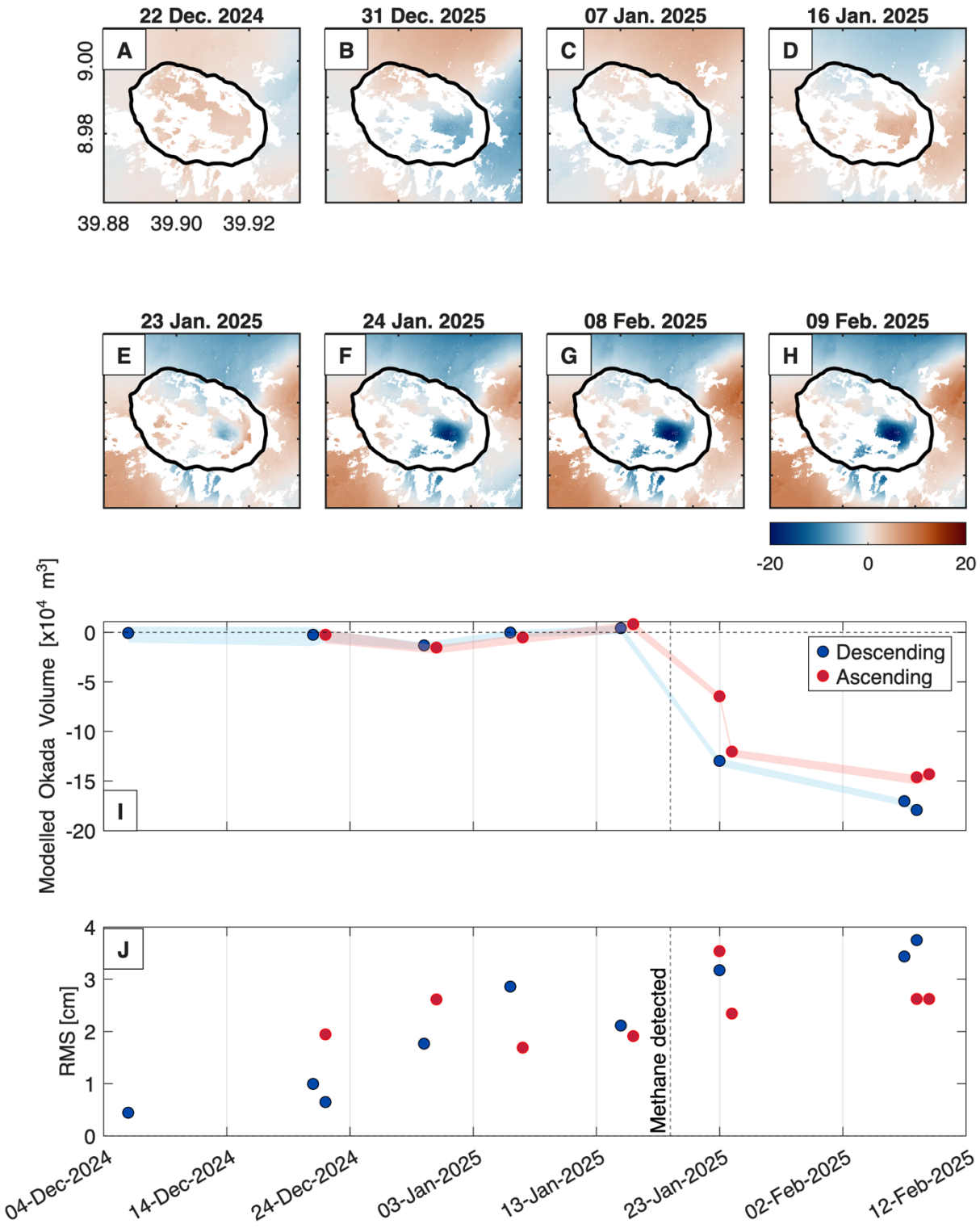

Figure S9. *Line-of-sight (LOS) displacement (cm) for all COSMO-SkyMed (CSK) ascending acquisition (A-H), showing the development of the localised subsidence signal in Fentale. Plots show the (I) estimated volume and (J) RMS extracted using the preferred model parameters (Sill; Table S8) for the localised subsidence in Fentale applied to all ascending (red) and descending (blue) CSK time steps.*

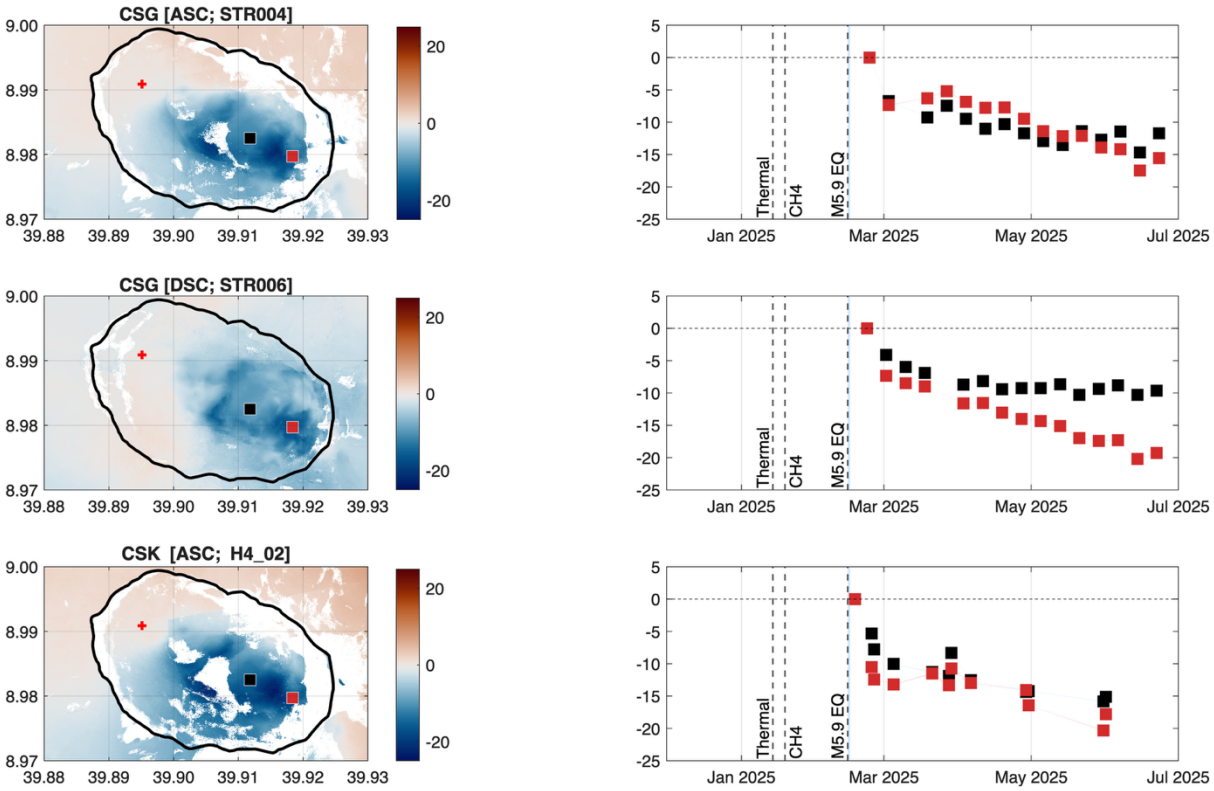

Figure S10. *Spatial and temporal displacement timeseries of Fentale crater following the large meter-scale collapse event on 14 February (17 Feb. to 23 Jun. 2025) for three Synthetic Aperture Radar (SAR) tracks. (Top row) ascending COSMO-SkyMed (CSK) Second Generation (CSG), (middle row) descending CSG and (bottom row) ascending CSK. Each row shows total spatial line-of-sight displacement (cm) and timeseries (red and black squares) show displacement through time for two locations (pixel location shown on spatial maps). Timeseries shows that deformation is largest on edge of crater collapse footprint with 10-15 cm deformation in February before the rate decreases. Reference pixel used shown as red cross on spatial maps. Deformation is cm-scale line-of-sight of the satellite.*

Supplementary Text 3 Evolution of the thermal anomaly

The first thermal anomaly on VIIRS was detected by TIRVolcH algorithm[13] on 14 January 2025 (22:48 UTC) approximately ~24 hours before the appearance of the low-lying white cloud (Fig. S11). From January to February, the thermal anomaly expanded and starting in March, we observe the migration of the hottest area towards the southeast (Fig. S12). Following this migration, the most intense thermal anomaly was located on the inner edge of the southeastern margin of the caldera, likely sourced by the steaming vents depicted in Figure S14. Concomitantly, a gradual decrease in the TIR-based Volcanic Radiative Power (VRP_{TIR}[14]) is observed, indicating that the diffuse degassing across the caldera was waning (Fig. S13).

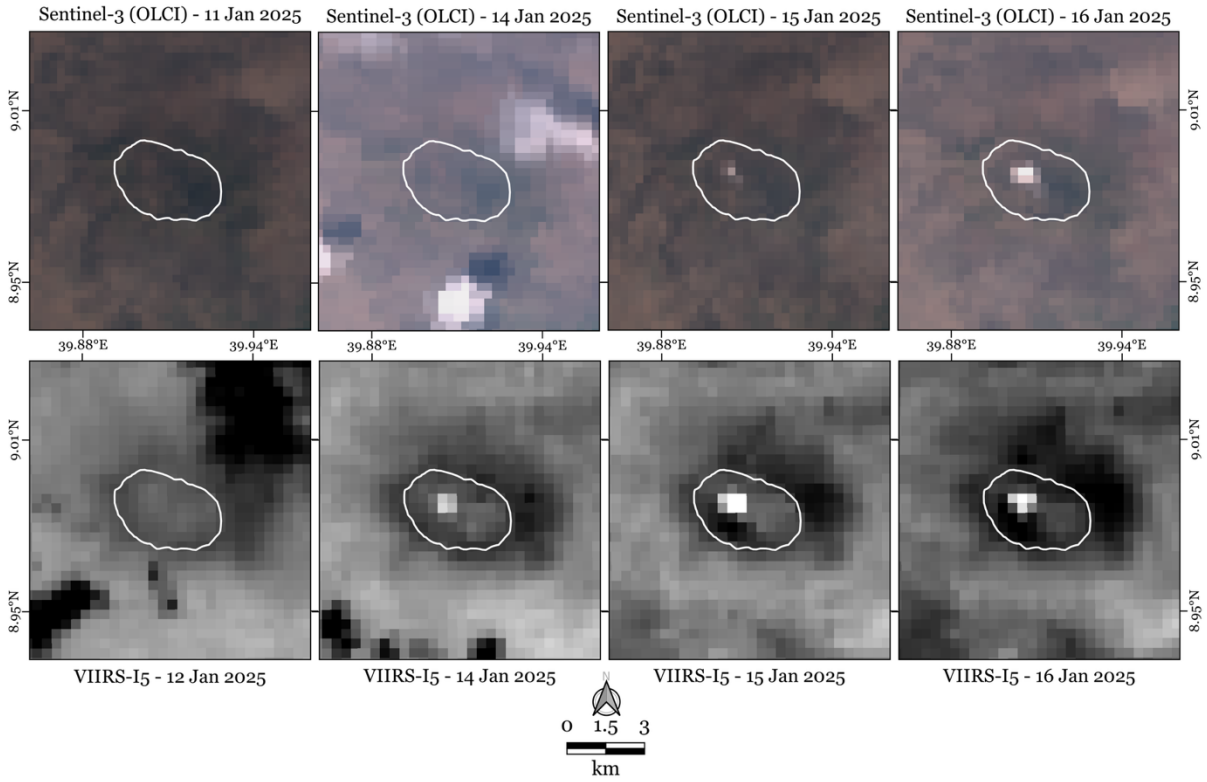

Figure S11. *Sentinel-3 (OLCI; top row) and VIIRS-I5 (TIR; bottom row) observations showing the first detection of the low-lying white cloud and thermal anomaly in Fentale crater.*

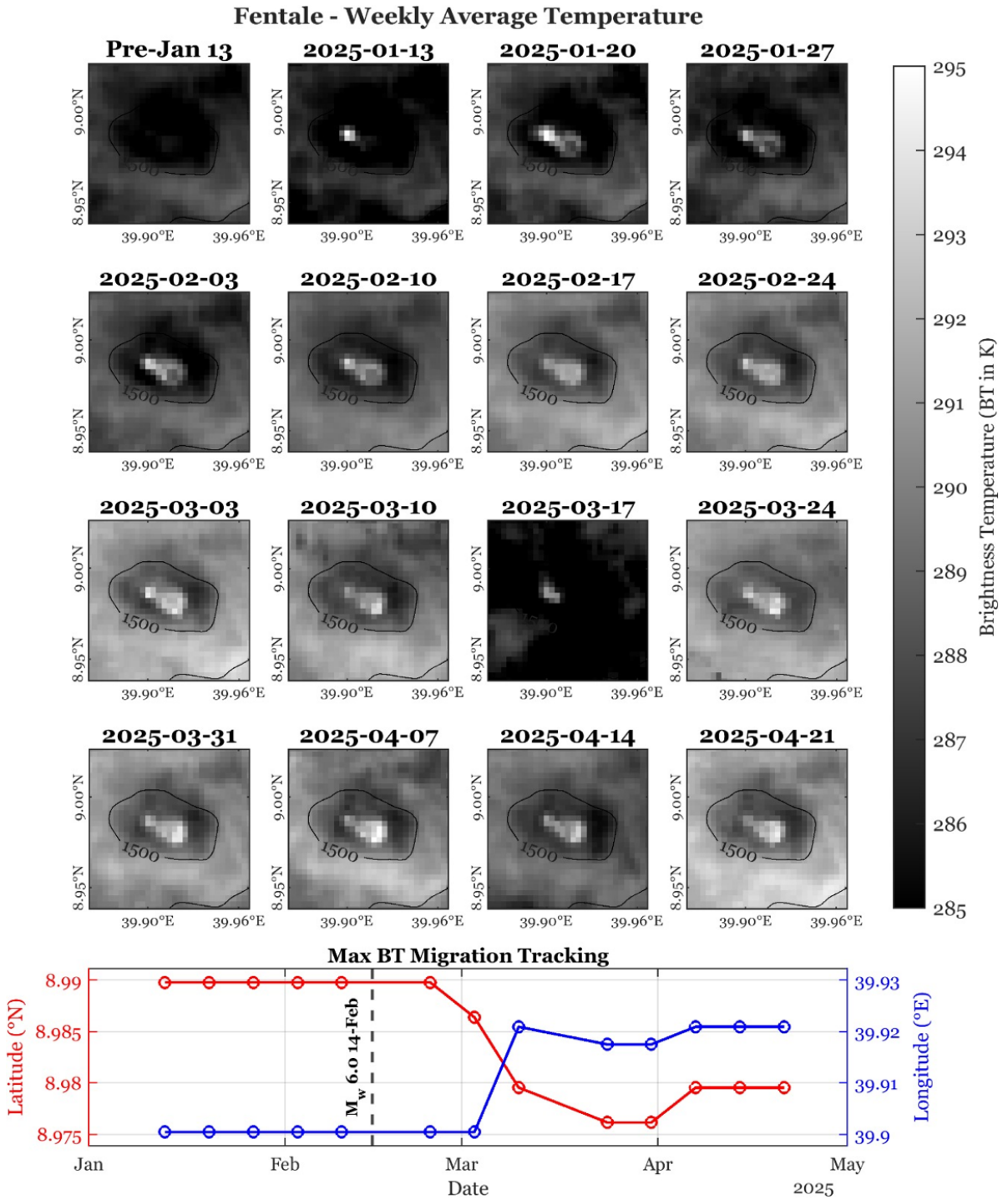

Figure S12. *VIIRS thermal imagery of the weekly average temperature over Fentale Volcano between January and April 2025, showing the spatial evolution of the thermal signal (localised, spreading and then migrating towards the southeast). Bottom panel shows the migration of the maximum brightness temperature for each timestep, showing the migration of the thermal anomaly in March 2025 toward the southeast.*

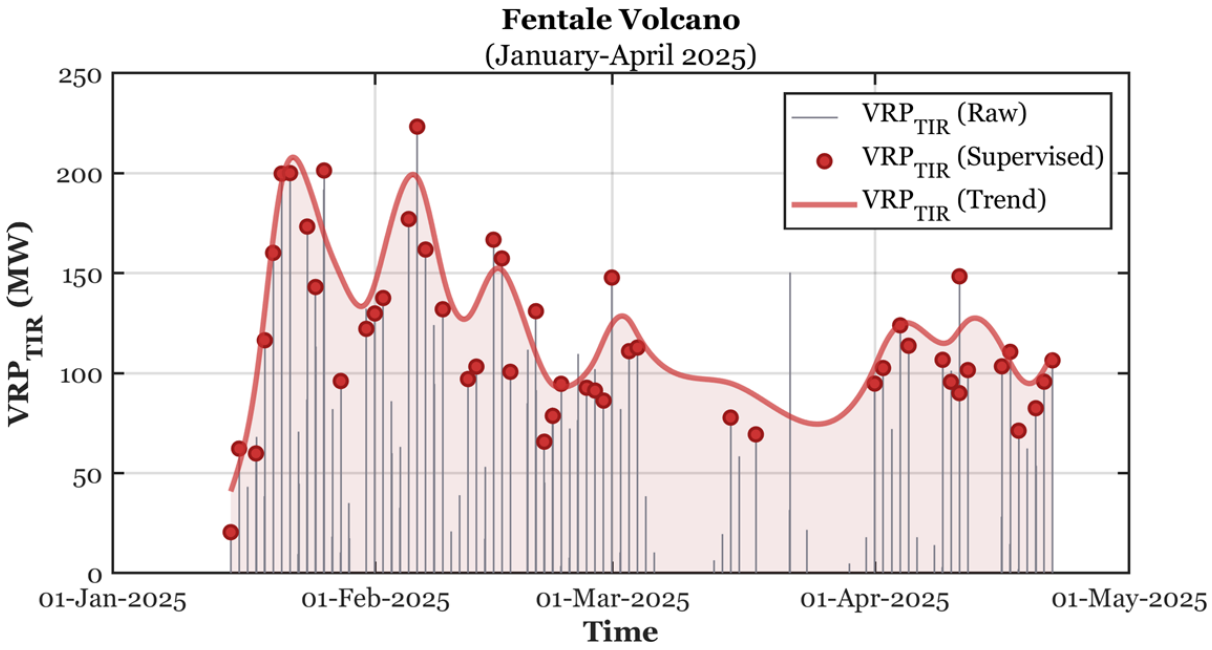

Figure S13. *Thermal anomaly timeseries (TIRVolcH-retireved VRP_{TIR}; TIR = Thermal Infrared; VRP = Volcanic Radiative Power) for Fentale, showing the sudden increase in January 2025 before reducing throughout February-April before stabilising. Thermal anomalies remain elevated following this unrest episode at Fentale.*

Supplementary Text 4 Optical imagery and Earthquake analysis

From Sentinel-2 and PlanetScope optical imagery we observe the appearance, growth and disappearance of a white cloud within Fentale crater from 17 January to 17 April (Fig. S14). There is no shadow visible associated with this cloud, indicating that it is relatively low-lying, which also allows us to differentiate it from meteorological cloud in non-cloud free images. The cloud first appears on 15 January 2025 (Sentinel-3, OLCI) situated in the lowest section of the caldera (a central depression). The cloud usually remained in the lowest sections of the caldera. We did observe variations in its spatial extent, with the cloud expanding to cover over half the caldera on 26 January. The largest spatial extent was observed following the first detection of methane gas (19 January). The overall temporal trend shows a gradual long-term decline in the area covered by this feature. We do observe small, short-lived expansions of the low-lying cloud in early February and another that correlated with the collapse event (14 February). Following the collapse event in mid-February, we observed steaming vents on the edge of the caldera. Unlike the low-lying cloud, these do produce shadows, indicating that they are moving to higher elevations. The last appearance of the low-lying cloud was on 17 April. Through March and April there was no persistent low-lying cloud present.

Coinciding with the start of the activity in Fentale crater in mid-January, we observe landslide deposits along the wall of the caldera in optical imagery (between 8-17 January). Although we do not observe an earthquake at Fentale coinciding with the beginning of this activity, there were many earthquakes in the Fentale-Dofen area over this time. The closest earthquake to Fentale before the thermal anomaly was detected was a M4.9 earthquake on 14 January 2025 (14:55 UTC) approximately 6-7 km southeast of Fentale (European-Mediterranean Seismological Centre, EMSC, catalogue).

Seismological analysis of the earthquake of 14 February 2025, at Fentale volcano

The source parameters for the earthquake of 14 February 2025 reported in the Global Centroid–Moment-Tensor (GCMT) catalog[15] indicate a relatively deep source, with a centroid depth of 19.5 km. The focal mechanism shows a large compensated-linear-vector-dipole (CLVD) component with a near-vertical compression (P) axis. The seismic scalar moment is reported as 1.21×10^{18} N-m, equivalent to moment magnitude M_W 6.0. We explore the parameter space associated with the GCMT inversion more fully, including evaluating the consistency of results obtained using subsets of the long-period seismic data included in the CMT analysis, and the extent to which a shallow crustal source is consistent with the data. Data in all frequency bands across the range used in the CMT analysis[15] prefer a depth in the range 18–20 km, and with remaining source parameters very similar to the preferred solution using all data. A shallow source fits the data less well. We also model broadband P and SH waves recorded globally for this event to obtain additional constraints on the source depth, moment-rate function, and focal mechanism. We follow the approach of Ekström (1989)[16], using our estimate of the point-source moment tensor from the CMT analysis and its covariance matrix as a soft constraint in the inversion, to obtain source models consistent with both the long-period data used in the CMT analysis and the broadband body waves. Again, we find preferred depths in the range 17–20 km, and poor fits to the data at shallow depths. The data are best explained by a moment-

rate function with a duration of 12–15 s, with two peaks separated by ~6 s. The broadband SH waves provide evidence for a complex source in which the focal geometry changes with time, likely because the fault strike changes with time; however, we are unable to resolve the details of the rupture progression.

The results of our seismological analysis are generally consistent with previous observations of earthquakes with a large CLVD component occurring in volcanic settings (e.g.,[17,18]), where the non-double-couple nature of the moment tensor results from rupture on a curved fault surface, such as the ring faults commonly observed under volcanoes[17–20]. When the rupture propagates around the arc of the ring fault, the focal geometry will change with time[19]. The source duration we obtain, of ~12 s, is approximately double that expected for earthquakes of similar moment[15], consistent with observations for volcanic CLVD earthquakes globally[18].

However, most volcanic CLVD earthquakes occur at shallower depths within the crust, typically in the top 10 km[17,18]. Our analysis suggests, though, that the greater depth of this earthquake is robust, consistent with the lack of obvious surface deformation from the earthquake in satellite data. Scaling relations[21] suggest a fault area of approximately 100 km^2 for an earthquake of this size, corresponding to a fault radius of ~5 km, and a fault slip of a few m. We therefore consider it unlikely that slip on the fault breached the very shallow source reservoir for the methane released at the time of the earthquake. Rather, the surface displacement or ground shaking caused by the earthquake may have led to further collapse of those near-surface reservoirs.

February crater collapse

We observe a collapse event in Fentale Caldera that coincides with the earthquake on 14 February 2025. Last pre-collapse observation was a COSMO-SkyMed Second Generation (CSG) image on 14 Feb 2025 (14:58 UTC). Optical cross-correlation combined with radar pixel offset tracking show that the motion of the collapse is predominantly vertical (approximately 40 m) with roughly a quarter coming from the horizontal component (~10 m towards west) (Fig. S15A-E).

The difference between two high-resolution DEM estimated a maximum collapse of ~40 m (mean collapse of 26 m) (Fig. S15F). Although this provides a more detailed spatial calculation of the collapse, it spans a much larger timeframe (09 January to 24 April 2025). Prior to (Fig. S7) and following (Fig. S10) the collapse, we observe cm-scale localised and widespread subsidence, producing roughly <1 m of subsidence in Fentale crater. Therefore, the majority of change observed in the DEM difference occurred in a short timeframe on the 14 February 2025. Initial estimates from combining optical and SAR imagery provided a rapid estimate during the event response (with similar magnitude) and covered a much shorter timeframe (07 February to 16 February 2025). However, these were lower resolution with higher uncertainties.

Mass Balance: Gas mass vs. volume change

To assess whether the ground deformation observed in January-February 2025 could account for the measured gas emissions from Fentale, we performed a simple mass balance calculation. The total volume change was taken as (1) the sum of the modelled volume change associated with the localised subsidence signal ($1.6\times10^5 \pm 3.2\times10^4$ m^3) and (2) the collapse volume extracted from the DEM differencing ($5.6\times10^7 \pm 5.2\times10^6$ m^3). The total gas mass was estimated from satellite-detected emission rates for methane (>38.2 ± 3.9 kt) and carbon dioxide (>2.9 ± 1.8 Mt). However, both represent minimum values due to limitations related to acquisition timing (i.e., onset of outburst not captured) and detection threshold (i.e., low emissions may have been missed). Assuming ideal gas behaviour at standard temperature and pressure, we calculate a gas concentration (concentration = mass/volume) of 52 ± 5 kg m^{-3} for the total volume observed. This value is an order of magnitude higher than expected. The density of a free gas under ideal conditions is typically ~1–2 kg m^{-3}, indicating a mass-volume mismatch. This mismatch between the observed volume change and detected gas mass suggest that the gases released during this outburst could not have solely originated from the shallow source we observed.

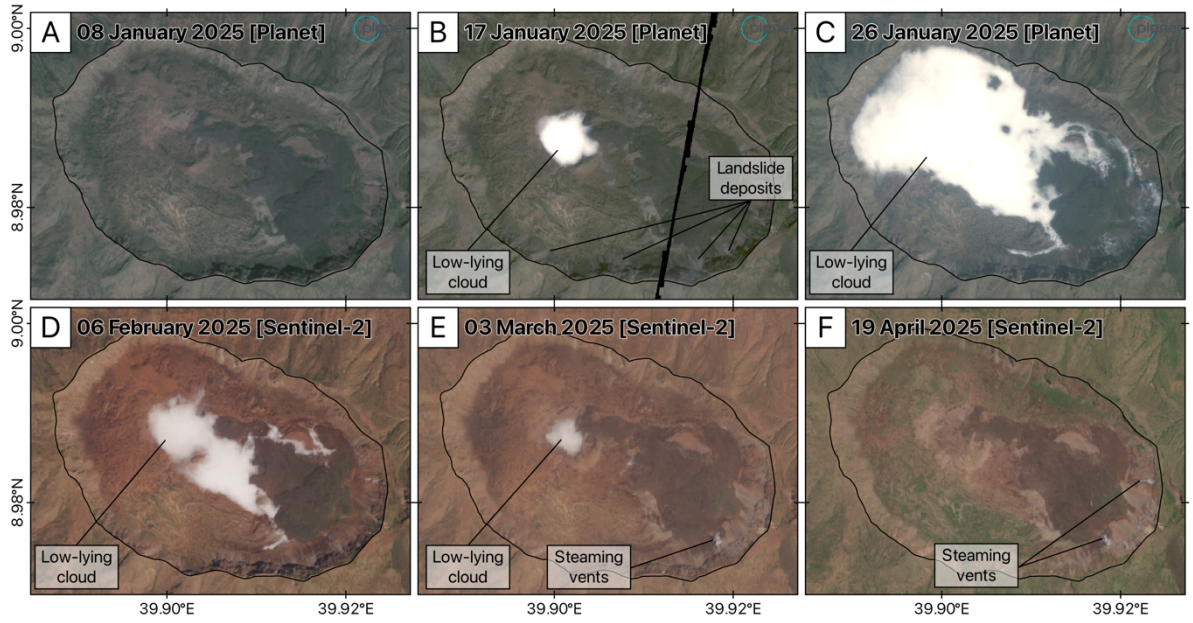

Figure S14 *PlanetScope and Sentinel-2 optical imagery over Fentale Caldera showing evolution of the low-lying white cloud between January and April 2025.*

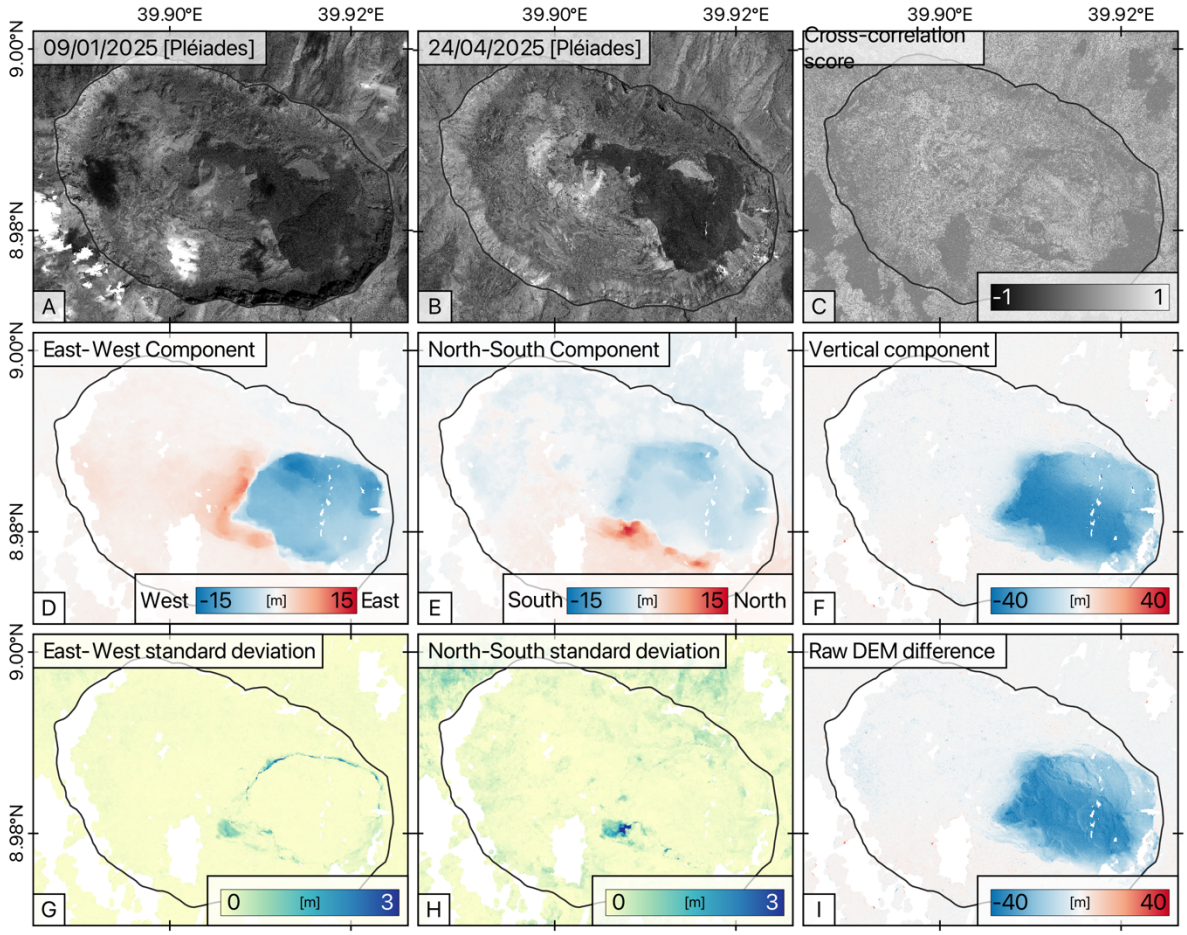

Figure S15. *Pléiades optical imagery acquired on 09 January 2025 and 24 April 2025 (a-b) spanning the M6.0 earthquake recorded on the 14 February 2025, UTC 20:28. Optical cross-correlation score (c) between the two Pléiades images. Horizontal surface displacement for (d) east-west component and (e) north-south component estimated from cross-correlation[22], with corresponding standard deviations (g-h). Vertical displacement (f) estimated from difference between the DEMs after correcting for the horizontal displacement. Raw DEMs difference (i). DEMs production, images orthorectification and optical cross-correlation were done using MicMac software[23].*

Supplementary Text 5 East African Rift (EAR) methane emission comparison

Here we compile gas chemistry data from sites across the Ethiopian and Kenyan rift, extracting those data that measure methane in fumaroles, bubbling and boiling pools, soil gas and geothermal wells. Methane (CH_4) concentrations are typically in the range of 1000-5000 ppm, although reaching 45% in bubbling pools at volcanoes (Fig. S16).

Methane concentrations of typical active volcanoes are mostly between 5 and 500 ppm (Fig. S16 and references therein), and therefore much lower than the those in Ethiopian and Kenyan rifts. However, methane concentrations in geothermal regions without recent surface volcanism (Fig. S15, e.g.,[24,25]) are comparable to the Ethiopian and Kenyan volcanoes. In these areas, methane is sourced from thermo-metamorphic/thermogenic processes, supporting the view that high methane contents of the Ethiopian volcanoes originate from the sedimentary systems rather than magma degassing.

We then combine the molar CO_2/CH_4 ratio and the CO_2 gas flux (where available) to estimate the total methane flux of typical Ethiopian and Kenyan volcanoes. It is important to note that the structural setting of these volcanoes (i.e. Aluto, Abaya, Tulu Moye) is different from Fentale. The former have large rift aligned tectonics faults, with large vertical offsets >100 m, dissecting the volcanic system[26,27], which are not observed at Fentale, suggesting it a closed system.

Using these fluxes, we estimate methane fluxes from the Ethiopian and Kenyan volcanoes to be 0.5–1 t d^{-1} (Table S9, Fig. S17). It important to note that the variability in CO_2/ CH_4 and uncertainty in CO_2 flux mean there is a large range in these estimates, and at some of the largest volcanic systems (i.e. Tulu Moye, which is much larger than Fentale), these fluxes likely exceed 1 t d^{-1}. Nevertheless, we can see that these estimates place the East African volcanoes among the largest methane emitters. This demonstrates that substantial volumes of methane are being emitted along the EARS.

Assuming that Aluto and Abaya are typical of highly permeable volcanic-geothermal systems (a reasonable assumption given the large tectonic faults that dissect the volcanoes), we can estimate how long it would have taken the methane release at Fentale to have accumulated. Given the 0.5–1 t d^{-1} rates of emission at these unsealed systems, the approximately 38 kt emitted by Fentale would have been accumulated over 100–200 years. The last eruption occurred in ~1810[28], so this would suggest that the hydrothermal system sealed relatively soon after the last eruption. Additionally, it is possible that the last eruption altered the plumbing system to allow gas to accumulate in the shallow subsurface.

Table S9. *Gas chemistry from volcanic sites across the Ethiopian and Kenyan rift. Estimates of methane (CH_4) emissions based on the CO_2/CH_4 ratio and CO_2 gas flux.*

Volcano	Molar CO_2/CH_4 [mean ± σ]	CO_2 flux [t d^{-1}]	CH_4 emission [t d^{-1}], mean [range]	References
Abaya, Ethiopia	108 ± 85	294 ± 71	1.0 [0.4–5.9]	Hutchison et al. (2023)[29]
Aluto, Ethiopia	283 ± 167	250–500	0.5 [0.2–1.6]	Regenspurg et al. (2022)[30] Hutchison et al. (2015, 2016)[31,32] Darling et al. (1998)[33]
Tulu Moye, Ethiopia (Salen range and Wordi)	46 ± 31	280–410	2.7 [1.3–10.1]	Assen et al. (in review)
Olkaria, Kenya	214 ± 176	~283	0.5 [0.3–2.7]	Darling et al. (1998)[33] Cappelli et al. (2023)[34]

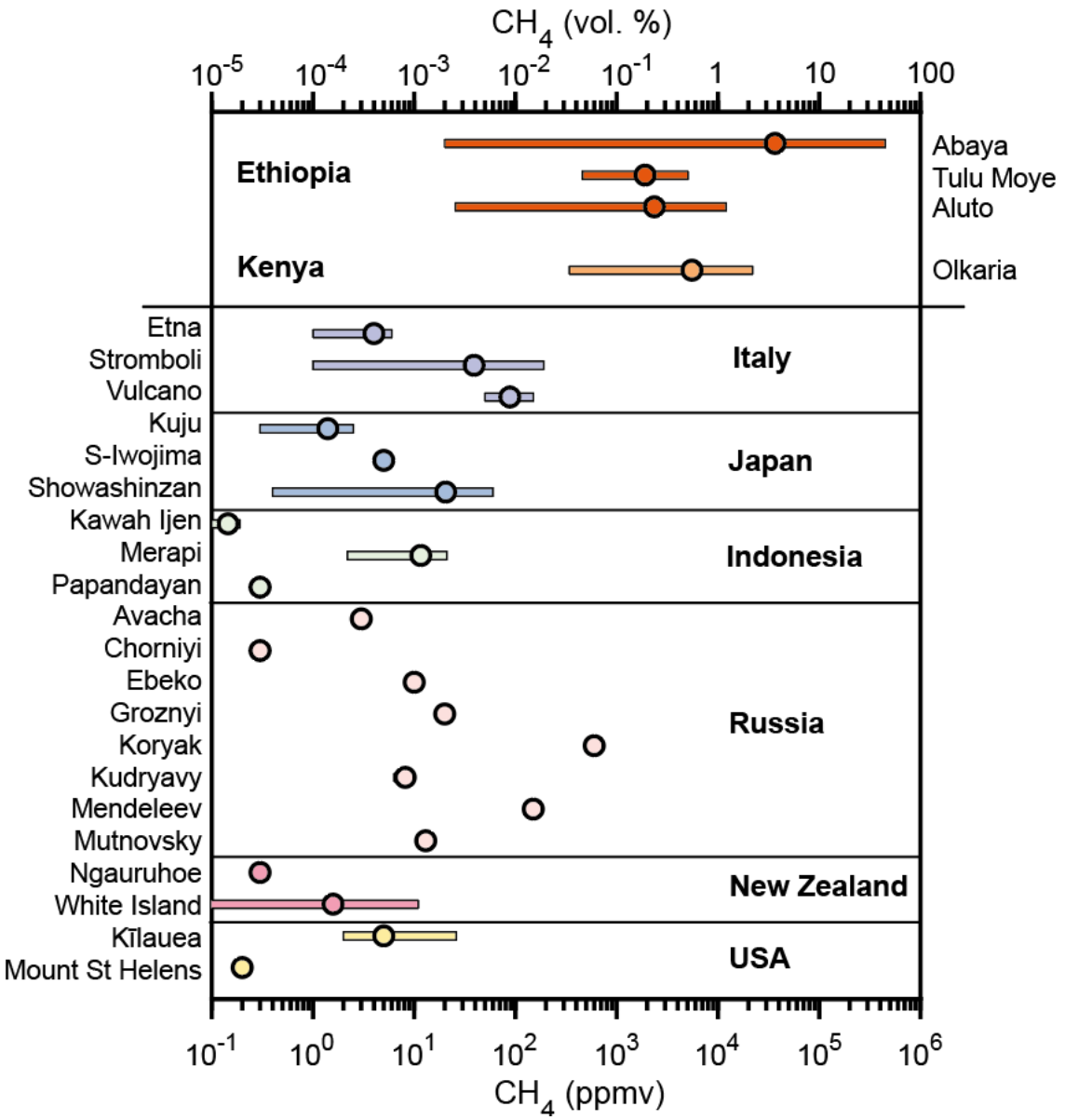

Figure S16: *Methane (CH_4) concentration of selected Ethiopian and Kenyan volcanoes and geothermal areas compared to other volcanic systems. East African data are from fumarole vents, hot springs and geothermal wells, while the those from volcanoes are mainly from fumaroles and wells. For each dataset the circle shows the mean value while the bar length corresponds to the minimum and maximum values (note that for many volcanoes only a single CH_4 concentration was available, i.e. no range could not be plotted). Data sources are as follows, Abaya: Hutchison et al. (2023); Minissale et al. (2017)[29,35], Tulu Moye: Assen et al. (in review), Aluto: Hutchison et al. (2015); Regenspurg et al. (2022)[30,31] and Olkaria: Darling et al. (1998)[33]. The other volcano CH_4 data are from fumarole and geothermal well samples and after Etiope et al. (2008); Hurwitz et al. (2003) and Taran and Giggenbach (2003) and references therein[36–38].*

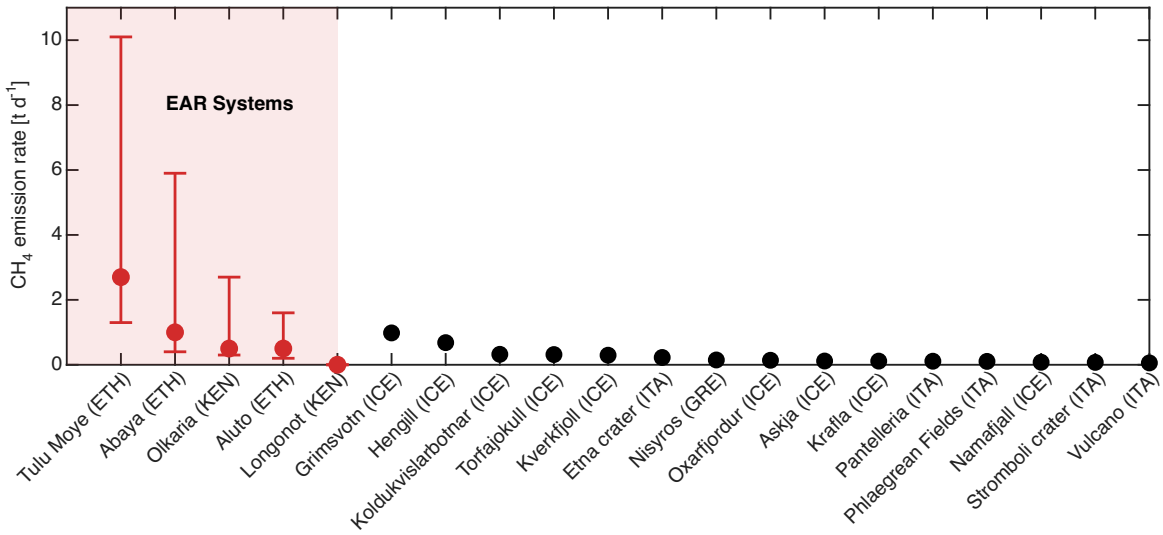

Figure S18. *Compilation of methane emission rates [t d^{-1}] for volcanic systems. Plot highlights the variability across the East African Rift (EAR) shown in red, generally showing elevated emission rates compared to volcanic systems globally. Emission rates for EAR systems shown in Table S9 and are compiled from Darling [29–34,39](1998), Robertson et al., 2016, Regenspurg et al. (2022), Hutchison et al. (2015, 2016, 2023), Cappelli et al. (2023), Assen et al. (in review) and global compilation is from Etiope et al., 2007[40].*

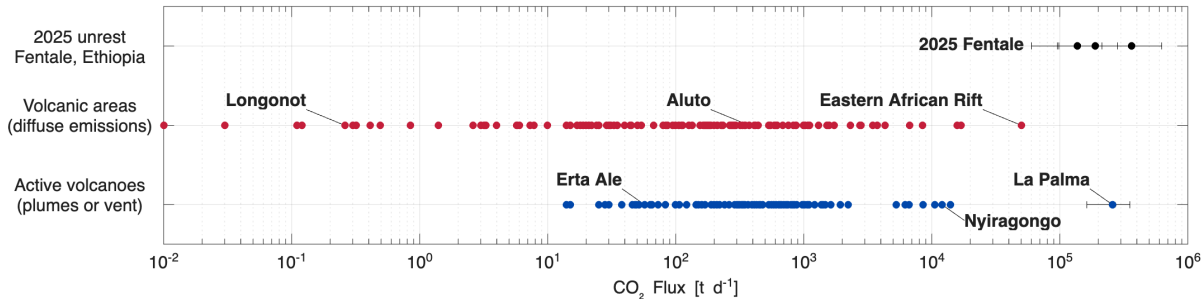

Figure S19. *Carbon dioxide flux comparison between the 2025 Fentale unrest event (black) estimated from Tanager-1, diffuse CO_2 emissions from active and dormant volcanic areas(red) and the CO_2 emission rates from active volcanoes released via plumes or vents and measured either directly or by satellites(blue). CO_2 fluxes from Table 1 and Table 3 in Werner et al. (2019)[41] and* Taquet et al. (2025)[42].

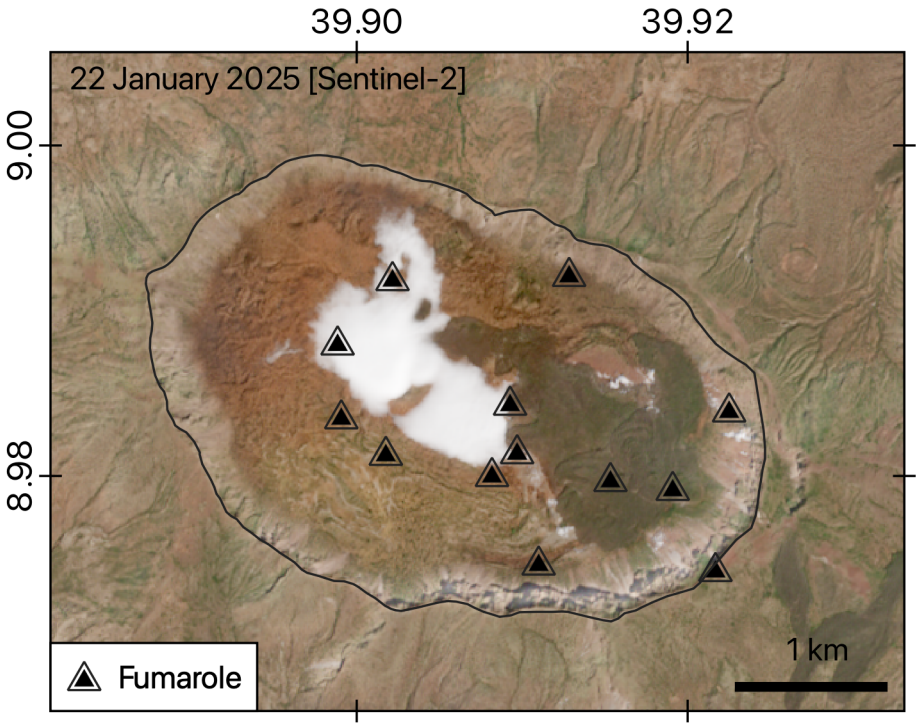

Figure S20. *Spatial distribution of fumaroles prior to the 2025 unrest event. Locations from Bekele et al. (2007)[43].*

References

1. Hersbach, H. *et al.* The ERA5 global reanalysis. *Quarterly Journal of the Royal Meteorological Society* 146, 1999–2049 (2020).
2. NCEP FNL, N. C. F. E. P. NCEP FNL Operational Model Global Tropospheric Analyses, continuing from July 1999. https://doi.org/10.5065/D6M043C6 (2000) doi:10.5065/D6M043C6.
3. Global Modeling and Assimilation Office Research. Global Modeling and Assimilation Office research: GEOS-FP version 5.21. *https://gmao.gsfc.nasa.gov/gmao-products/geos-fp/geos-fp-version-521-details_geos-fp/* https://gmao.gsfc.nasa.gov/gmao-products/geos-fp/geos-fp-version-521-details_geos-fp/ (2025).
4. Hong, S. Y., Noh, Y. & Dudhia, J. A New Vertical Diffusion Package with an Explicit Treatment of Entrainment Processes. *Mon Weather Rev* 134, 2318–2341 (2006).
5. Janjić, Z. I. The Step-Mountain Eta Coordinate Model: Further Developments of the Convection, Viscous Sublayer, and Turbulence Closure Schemes. *Mon Weather Rev* 122, 927–945 (1994).
6. Sukoriansky, S., Galperin, B. & Perov, V. Application of a new spectral theory of stably stratified turbulence to the atmospheric boundary layer over sea ice. *Boundary Layer Meteorol* 117, 231–257 (2005).
7. Nakanishi, M. & Niino, H. An improved Mellor-Yamada Level-3 model: Its numerical stability and application to a regional prediction of advection fog. *Boundary Layer Meteorol* 119, 397–407 (2006).

8. Giudicepietro, F. *et al.* First evidence of a geodetic anomaly in the Campi Flegrei caldera (Italy) ground deformation pattern revealed by DInSAR and GNSS measurements during the 2021–2023 escalating unrest phase. *International Journal of Applied Earth Observation and Geoinformation* 132, 104060 (2024).
9. Okada, Y. SURFACE DEFORMATION DUE TO SHEAR AND TENSILE FAULTS IN A HALF-SPACE. *Bulletin of the Seismological Society of America* 75, 1135–1154 (1985).
10. Sun, R. J. Theoretical size of hydraulically induced horizontal fractures and corresponding surface uplift in an idealized medium. *J Geophys Res* 74, 5995–6011 (1969).
11. Mogi, K. Relations between the eruptions of various volcanoes and the deformations of the ground surfaces around them. *Bulletin of the Earthquake Research Institute* 36, 99–134 (1958).
12. Cervelli, P. F., Cervelli & F., P. Analytical Expressions for Deformation from an Arbitrarily Oriented Spheroid in a Half-Space. *AGUFM* 2013, V44C-06 (2013).
13. Aveni, S., Laiolo, M., Campus, A., Massimetti, F. & Coppola, D. TIRVolcH: Thermal Infrared Recognition of Volcanic Hotspots. A single band TIR-based algorithm to detect low-to-high thermal anomalies in volcanic regions. *Remote Sens Environ* 315, 114388 (2024).
14. Aveni, S., Pailot-Bonnétat, S., Rouwet, D., Harris, A. J. L. & Coppola, D. Volcanic Radiative Power Retrieval From Moderate-to-Low-Temperature Features Using a Single TIR Band: Validation Using Volcanic Crater Lakes and Hydrothermal Systems. *Geophys Res Lett* 52, e2024GL113324 (2025).
15. Ekström, G., Nettles, M. & Dziewoński, A. M. The global CMT project 2004–2010: Centroid-moment tensors for 13,017 earthquakes. *Physics of the Earth and Planetary Interiors* 200–201, 1–9 (2012).
16. Ekström, G. A very broad band inversion method for the recovery of earthquake source parameters. *Tectonophysics* 166, 73–100 (1989).
17. Shuler, A., Ekström, G. & Nettles, M. Physical mechanisms for vertical-CLVD earthquakes at active volcanoes. *J Geophys Res Solid Earth* 118, 1569–1586 (2013).
18. Shuler, A., Nettles, M. & Ekström, G. Global observation of vertical-CLVD earthquakes at active volcanoes. *J Geophys Res Solid Earth* 118, 138–164 (2013).
19. Nettles, M. & Ekström, G. Faulting mechanism of anomalous earthquakes near Bárdarbunga Volcano, Iceland. *J Geophys Res Solid Earth* 103, 17973–17983 (1998).
20. Ekström, G. Anomalous earthquakes on volcano ring-fault structures. *Earth Planet Sci Lett* 128, 707–712 (1994).
21. Kanamori, H. & Anderson, D. L. Theoretical Basis of some Empirical Relations in Seismology. *Bulletin of the Seismological Society of America* 65, 1073–1095 (1975).
22. Hauck, A., Grandin, R. & Delorme, A. Horizontal deformation in Fentale caldera associated with 14 February 2025 earthquake. *Earth System Data Repository (EaSY DATA)* https://www.easydata.earth/#/public/metadata/b4ce1bad-a61b-499a-a3aa-36b632f45e56 (2025).
23. Rosu, A. M., Pierrot-Deseilligny, M., Delorme, A., Binet, R. & Klinger, Y. Measurement of ground displacement from optical satellite image correlation using the free open-source software MicMac. *ISPRS Journal of Photogrammetry and Remote Sensing* 100, 48–59 (2015).

24. Tassi, F., Fiebig, J., Vaselli, O. & Nocentini, M. Origins of methane discharging from volcanic-hydrothermal, geothermal and cold emissions in Italy. *Chem Geol* 310–311, 36–48 (2012).
25. Zhou, X., Liu, L., Chen, Z., Cui, Y. & Du, J. Gas geochemistry of the hot spring in the Litang fault zone, Southeast Tibetan Plateau. *Applied Geochemistry* 79, 17–26 (2017).
26. Hunt, J. A., Zafu, A., Mather, T. A., Pyle, D. M. & Barry, P. H. Spatially Variable CO2 Degassing in the Main Ethiopian Rift: Implications for Magma Storage, Volatile Transport, and Rift-Related Emissions. *Geochemistry, Geophysics, Geosystems* 18, 3714–3737 (2017).
27. Maestrelli, D., Corti, G., Bonini, M., Montanari, D. & Sani, F. Caldera collapse and tectonics along the Main Ethiopian Rift: reviewing possible relationships. *Comptes Rendus. Géoscience* 353, 91–109 (2022).
28. Williams, F. M., Williams, M. A. J. & Aumento, F. Tensional fissures and crustal extension rates in the northern part of the Main Ethiopian Rift. *Journal of African Earth Sciences* 38, 183–197 (2004).
29. Hutchison, W. *et al.* Gas Emissions and Subsurface Architecture of Fault-Controlled Geothermal Systems: A Case Study of the North Abaya Geothermal Area. *Geochemistry, Geophysics, Geosystems* 24, e2022GC010822 (2023).
30. Regenspurg, S. *et al.* Origin and migration of fluoride in the area of the Aluto Volcanic Complex (Main Ethiopian Rift). *Applied Geochemistry* 146, 105403 (2022).
31. Hutchison, W., Mather, T. A., Pyle, D. M., Biggs, J. & Yirgu, G. Structural controls on fluid pathways in an active rift system: A case study of the Aluto volcanic complex. https://doi.org/10.1130/GES01119.1 (2015) doi:10.1130/GES01119.1.
32. Hutchison, W. *et al.* The eruptive history and magmatic evolution of Aluto volcano: new insights into silicic peralkaline volcanism in the Ethiopian rift. *Journal of Volcanology and Geothermal Research* 328, 9–33 (2016).
33. Darling, W. G. Hydrothermal hydrocarbon gases: 2, Application in the East African Rift System. *Applied Geochemistry* 13, 825–840 (1998).
34. Cappelli, L. *et al.* Diffuse soil CO2 emissions at rift volcanoes: Structural controls and total budget of the Olkaria Volcanic Complex (Kenya) case study. *Journal of Volcanology and Geothermal Research* 443, 107929 (2023).
35. Minissale, A. *et al.* Geothermal potential and origin of natural thermal fluids in the northern Lake Abaya area, Main Ethiopian Rift, East Africa. *Journal of Volcanology and Geothermal Research* 336, 1–18 (2017).
36. Hurwitz, S., Kipp, K. L., Ingebritsen, S. E. & Reid, M. E. Groundwater flow, heat transport, and water table position within volcanic edifices: Implications for volcanic processes in the Cascade Range. *J Geophys Res Solid Earth* 108, 2557 (2003).
37. Etiope, G., Lassey, K. R., Klusman, R. W. & Boschi, E. Reappraisal of the fossil methane budget and related emission from geologic sources. *Geophys Res Lett* 35, (2008).
38. Taran, Y. A. & Giggenbach, W. F. Geochemistry of Light Hydrocarbons in Subduction-Related Volcanic and Hydrothermal Fluids. *Volcanic, Geothermal, and Ore-Forming Fluids* 61–74 (2005) doi:10.5382/SP.10.04.
39. Robertson, E. *et al.* Diffuse degassing at Longonot volcano, Kenya: Implications for CO2 flux in continental rifts. *Journal of Volcanology and Geothermal Research* 327, 208–222 (2016).

40. Etiope, G., Fridriksson, T., Italiano, F., Winiwarter, W. & Theloke, J. Natural emissions of methane from geothermal and volcanic sources in Europe. *Journal of Volcanology and Geothermal Research* 165, 76–86 (2007).
41. Werner, C. *et al.* Carbon Dioxide Emissions from Subaerial Volcanic Regions: Two Decades in Review. in *Deep Carbon. Past to Present* 188–236 (Cambridge University Press, 2019).
42. Taquet, N. *et al.* Volatile emissions during the 2021 Cumbre Vieja (La Palma) eruption integrating multiplatform atmospheric observations. *Atmos Chem Phys* 25, 14591–14628 (2025).
43. Bekele, B., Mamo, T., Teclu, A. & Kebede, Y. Compilation of the geoscientific study of the Dofan-Fantale Geothermal Prospect, Ethiopia. *Ministry of Mines and Energy and Geological Survey of Ethiopia* (2007).